Journal of Systems Engineering and Electronics
Vol. 33, No. 3, June 2022, pp.522 – 533

Unintentional modulation microstructure enlargement

SUN Liting, WANG Xiang*, and HUANG Zhitao

Department of Electronic Science, National University of Defense Technology, Changsha 410073, China

Abstract: Radio frequency fingerprinting (RFF) is a technology that identifies the specific emitter of a received electromagnetic signal by external measurement of the minuscule hardware-level, device-specific imperfections. The RFF-related information is mainly in the form of unintentional modulation (UIM), which is subtle enough to be effectively imperceptible and is submerged in the intentional modulation (IM). It is necessary to minimize the influence of the IM and expand the slight differences between emitters for successful RFF. This paper proposes a UIM microstructure enlargement (UMME) method based on feature-level adaptive signal decomposition (ASD), accompanied by autocorrelation and cross-correlation analysis. The common IM part is evaluated by analyzing a newly-defined benchmark feature. Three different indexes are used to quantify the similarity, distance, and dependency of the RFF features from different devices. Experiments are conducted based on the real-world signals transmitted from 20 of the same type of radar in the same working mode. The visual image qualitatively shows the magnification of feature differences; different indicators quantitatively describe the changes in features. Compared with the original RFF feature, recognition results based on the Gaussian mixture model (GMM) classifier further validate the effectiveness of the proposed algorithm.

Keywords: radio frequency fingerprinting (RFF), unintentional modulation (UIM), adaptive signal decomposition (ASD), variational mode decomposition (VMD), similarity measurement.

DOI: 10.23919/JSEE.2022.000052

1. Introduction

Radio frequency fingerprint is a characteristic intrinsic to the hardware chain of an emitter device, that is unntentionally modulated to transmitted signals, and thus can be leveraged to discriminate the specific transmitter [1]. Radio frequency fingerprinting (RFF), also known as specific emitter identification (SEI), has a wide range of applications in wireless network security [2−4], cognitive radio [3,5], and spectrum management [6]. A typical RFF system is illustrated [7].

The core of the RFF system is the effective discriminative feature [8,9]. Many previous researchers have explored RFF features, which can be roughly divided into time-domain [10,11], frequency-domain [12,13], time-frequency domain [14−16], and other transformation-domain categories [17−19]. Recently proposed methods based on deep learning (DL) have become increasingly attractive [18,20,21]. However, these algorithms mainly focus on extracting newly defined manual or automatic features, rather than exploring the common distribution characteristics of the existing RFF features and improving their performance.

More specifically, little attention has been paid to unintentional modulation (UIM). For emitters with the same intentional modulation (IM) on pulse, the identification-relevant device-specific information of RFF is UIM, mainly caused by manufacturing tolerances and aging of the equipment in the transmitter [12,22,23]. However, the individual differences are so subtle that they are effectually imperceptible; they are also submerged in the useless main information, IM, which may be harmful to RFF [24].

Although UIM is hard to extract, researchers have succeeded in separating it. In [5], the estimated ideal IM can be directly subtracted from the time domain to obtain time-domain complex baseband error signals was obtained. Detailed estimation of all various modulation parameters is difficult, however, and the resulting estimation errors markedly affect the UIM features [12]. A primary signal suppression method based on wavelet transform was proposed [25]. And IM parameters were estimated and then compensated [19]. The shared features and private features were separated at the signal level by a discriminative adversarial networks (DAN) [26], which is effective but requires a large amount of learning data.

Existing algorithms work by extracting UIM directly from the original data waveform at the signal level. There is an excess of influencing factors in these cases, however, which makes subsequent analysis very difficult. IM may

Manuscript received February 04, 2021.
*Corresponding author.
This work was supported by the Program for Innovative Research Groups of the Hunan Provincial Natural Science Foundation of China (2019JJ10004).

be reflected as the overall similarity of feature curves at the feature level [12,23]. As UIM features are relatively weak, it is necessary to enlarge the subtle fingerprint features to conduct a successful analysis.

Motivated by these thoughts, we mainly focus on the feature extraction phase of the system in this study, establish a technique based on adaptive signal decomposition (ASD) to analyse the components of RFF features, eliminate the IM, and enlarge the UIM microstructure at the feature level to optimize the existing RFF features.

ASD, also known as "local wave decomposition", has been widely applied in several research fields [27,28]. For RFF problems, ASD is usually used to directly decompose the time-domain waveform of individual signals and further extract new fingerprint features rather than distinguishing UIM [14,15,22]. Liang et al. [29] used empirical mode decomposition to obtain stray components. However, the eliminated main component varies among signals; it is not strictly the common IM of all emitters, therefore device-specific information may be lost. Existing methods also are restricted to the signal level.

In this paper, variational mode decomposition (VMD), a newly proposed ASD method, is used to adaptively decompose the autocorrelation of benchmark features to obtain different components. We integrate correlation calculation into this process to amplify subtle structural differences and eliminate shared major components. We strictly control variables, delete the same components from different samples, and minimize the loss of effective information accordingly. The major contributions of this work can be summarized as follows:

(i) An innovative UIM microstructure enlargement (UMME) technique is established for RFF. It is the first attempt to specifically eliminate the IM at the feature level and amplify subtle fingerprint features to optimize the specific emitter identification.

(ii) Benchmark feature is defined and implemented to describe the main common information shared by all emitters. The correlation calculation is ingeniously introduced into RFF to amplify subtle inter-class differences based on the benchmark features.

(iii) Inspired by the mechanism of RFF, that is, RFF features contain both the emitter-specific UIM and the emitter-shared IM, ASD is used to analyze different feature components, namely, the main trends and the stray high-frequency items.

(iv) Three different indicators are introduced to measure the effect of RFF feature difference amplification, including Pearson product-moment correlation coefficient (PE), euclidean distance (ED), and mutual information (MI). Visual and numerical results on real-world dataset prove that the subtle UIM differences are effectively magnified. The algorithm is validated by an improved classification recognition rate.

The rest of this paper is organized as follows: Section 2 briefly describes the UIM signal model, the calculation process of VMD, and three evaluation indexes for subtle UIM differences. In Section 3, the detailed implementation of the proposed algorithm is given. Section 4 provides the visual and numerical results. Section 5 presents a conclusions.

2. Problem formulation

2.1 Signal model of RFF mechanism

Theoretically, the signals of the same modulation, transmitted from the same kind of emitter and processed by the same pre-procedure, have similar feature shapes [12,23]. This is precisely the case in a real-world scenario. IM is the major component of a signal and is manifested in the common characteristics of signals with the same parameters from various emitters used for SEI. UIM, conversely, is caused by imperfections in different emitters; it has lower energy than IM, and is manifested in the stable differences associated with individuals [24].

Let S^m and UIM^m denote the whole and UIM part of the mth emitter, the signal model of the aforementioned analysis can be expressed as

$$S^m = \mathrm{IM} + \mathrm{UIM}^m, \quad m = 1, 2, \cdots, M \tag{1}$$

where M is the number of the emitters and IM represents the common IM part belonging to all of the emitters.

UIM appears as a series of slight differences among signals from various emitters in many signal processing domains, which is usually embodied in the signals' microstructures. The differences between transmitters are random and independent. UIM tends to be obscured by IM and thus very difficult to extract. It also satisfies the energy relationship $\mathrm{IM} \gg \mathrm{UIM}^m$.

Theoretically, as long as there are sufficient signal observations accumulated and analyzed, the general distribution rule of the IM can be obtained by its sufficient statistic [30], as follows:

$$\lim_{M\to\infty} \frac{1}{M} \sum_{m=1}^{M} S^m \approx \mathrm{IM}. \tag{2}$$

In practice, however, UIM cannot be directly derived by subtracting the accumulation of original features IM owing to its inherent diversity and low energy. The UIM microstructure must be extracted and enlarged in a particular manner to properly analyze it.

2.2 Knowledge of VMD

VMD technique decomposes a multi-component signal

into a set of intrinsic mode functions (IMFs) non-recursively [31]. Essentially, it is the construction and solving of a variational problem, assuming that the non-linear and non-stationary signals are formed by the superposition of several mode functions. Each IMF obtained after VMD is band-limited, and can be represented as a narrow-band signal with amplitude modulation-frequency modulation (AM-FM) in different center frequencies.

The IMF u_k is given by

$$u_k = A_k(t)\cos(\phi_k(t)) \tag{3}$$

where A_k is the instantaneous amplitude satisfying $A_k \geqslant 0$, ϕ_k is the increasing phase function, and $\omega_k(t) = \phi_k'(t)$ is the instantaneous frequency.

VMD can be converted into a constrained variational problem as follows:

$$\min_{u_k,\omega_k}\left\{\sum_k\left\|\partial_t\left[\left(\delta(t)+\frac{\mathrm{j}}{\pi t}\right)*u_k(t)\right]\mathrm{e}^{-\mathrm{j}\omega kt}\right\|_2^2\right\}$$
$$\text{s.t.}\ \sum_k u_k(t) = f(t) \tag{4}$$

where u_k is the kth mode, $f(t)$ is the original signal to be decomposed, ω_k is the corresponding center frequency, $\delta(t)$ is the impulse function, ∂_t is the gradient with respect to t, and $*$ represents the convolution operation.

The secondary penalty parameter α and augmented Lagrange multiplier $\lambda(t)$ are introduced to solve the aforementioned constrained variational problem. The quadratic penalty parameter α makes the variational dispersion problem highly nonlinear and non-convex, which ensures that the signal can be decomposed accurately under the Gaussian noise. The Lagrange multiplier $\lambda(t)$ guarantees the strictness of obtaining the optimal bandwidth solution per IMF. The squared l_2-norm of the base-band-shifted Hilbert analytic function with non-negative frequencies reveals the bandwidth of each mode [24].

After introducing α and $\lambda(t)$, the constraint variational problem can be converted into an unconstrained variational problem as follows:

$$L = (\{u_k\},\{\omega_k\},\lambda) =$$
$$\alpha\sum_k\left\|\partial_t\left[\delta(t)+\frac{\mathrm{j}}{\pi t}*u_k(t)\right]\mathrm{e}^{-\mathrm{j}\omega kt}\right\|^2 +$$
$$\left\|f(t)-\sum_k u_k\right\|_2^2 + \left\langle\lambda(t), f(t)-\sum_k u_k\right\rangle \tag{5}$$

where $\langle\cdot\rangle$ represents the inner product operation.

Next, u_k, ω_k, and λ are iteratively updated by using the alternating direction multiplier method to solve the saddle points of the upper augmented Lagrange function. This equals the optimal solution of the constrained variational model. The decomposed modes and their center frequencies can be obtained from the solution. The modes in the spectral domain can be given as

$$\hat{u}_k(\omega) = \frac{\hat{f}(\omega)-\sum_{j\neq k}\hat{u}_k+(\hat{\lambda}(\omega))/2}{1+2\alpha(\omega-\omega_k)^2}. \tag{6}$$

The sequence of the specific steps involved in VMD can be summarized as follows:

Step 1 Update mode

The modes are updated in the Fourier domain. Conversely, the mode in the time domain is obtained as the real part of the inverse Fourier transform of this filtered analytic signal.

$$\hat{u}_k^{n+1}(\omega) = \frac{\hat{f}(\omega)-\sum_{j\neq k}\hat{u}_k^n+(\hat{\lambda}^n(\omega))/2}{1+2\alpha(\omega-\omega_k^n)^2} \tag{7}$$

Step 2 Update center frequency

Again, the optimization takes place in the Fourier domain, and we end up calculating,

$$\omega_k^{n+1} = \frac{\int_0^\infty \omega|\hat{v}_k(\omega)|^2\mathrm{d}\omega}{\int_0^\infty|\hat{v}_k(\omega)|^2\mathrm{d}\omega} \tag{8}$$

where the new ω_k falls at the center of gravity of the corresponding mode's power spectrum.

Step 3 Cyclic processing

Repeat Step 1 and Step 2 until the number of modes equals the present value K.

Step 4 Update multiplier

Update the Lagrange multiplier as follows:

$$\hat{\lambda}^{n+1} = \hat{\lambda}^n + \tau\left(\hat{f}-\sum_k\hat{u}_k^{n+1}\right) \tag{9}$$

where $\hat{f}$ is the spectrum of the signal and $\hat{u}_k$ is the spectrum of the kth mode.

Step 5 Check convergence conditions

If $\sum_k\left\|\hat{u}_k^{n+1}-\hat{u}_k^n\right\|_2^2/\left\|\hat{u}_k^n\right\|_2^2 < \varepsilon$, the calculation results including all IMFs, center frequencies, and spectra of the modes are output; otherwise, return to Step 1.

2.3 Evaluation index

We choose three measurements to evaluate the similarity, distance, and dependency of RFF features.

2.3.1 PE

PE reflects the degree of linear correlation between two variables X and Y as a measure of the similarity between curve shapes [32]. The value of PE is between −1 and 1. The curves in question are more similar when the absolute

PE is close to 1, and less similar when it is closer to 0. The PE of X and Y can be expressed as

$$\mathrm{PE}=\frac{\mathrm{E}(XY)-\mathrm{E}(X)\mathrm{E}(Y)}{\sqrt{\mathrm{E}\left(X^2\right)-\mathrm{E}^2(X)}\sqrt{\mathrm{E}\left(Y^2\right)-\mathrm{E}^2(Y)}}=\frac{\mathrm{E}((X-\mu_X)(Y-\mu_Y))}{\sigma_X\sigma_Y}=\frac{\mathrm{cov}(X,Y)}{\sigma_X\sigma_Y} \tag{10}$$

where E{·} denotes the mean operator, μ denotes the average, σ is the variance, and cov(X,Y) is the covariance.

2.3.2 ED

ED is a common distance measurement tool for patten recognition; it has translation invariance and rotation invariance [33]. ED facilitates classification in techniques such as the K-nearest neighbors (KNN) algorithm. We use ED to analyze the distribution characteristics of RFF features:

$$\mathrm{ED}=d(X,Y)=\sqrt{\sum_{i=1}^{n}(x_i-y_i)^2}. \tag{11}$$

2.3.3 MI

In information theory, MI is a measure of the interdependence between two random variables. If the joint distribution of two random variables (X,Y) is $p(x_iy_i)$, then MI is

$$\mathrm{MI}=\sum_{y_i\in Y}\sum_{x_i\in X}p(x_iy_i)\log_2\frac{p(x_iy_i)}{p(x_i)p(y_i)}. \tag{12}$$

3. Algorithm implementation

The typicle RFF system is shown in Fig. 1. The curve of the RFF system is the procedure of feature extraction. The implementation of the proposed method consists of two phases: feature component analysis of the benchmark feature and microstructure enlargement of each original feature, as is shown in Fig. 2. The upper branch in the flow chart represents the feature component analysis stage, including benchmark feature calculation, feature autocorrelation, VMD, and IMF acquisition of different types of IMF. On the other hand, the UIM-related microstructure enlargement involves calculating the cross-correlation between the original feature and the benchmark feature, then removing the IMFs unrelated to individual information or of high frequency to obtain the final feature. The final feature is marked as "UMME".

The key steps of the scheme are described in detail.

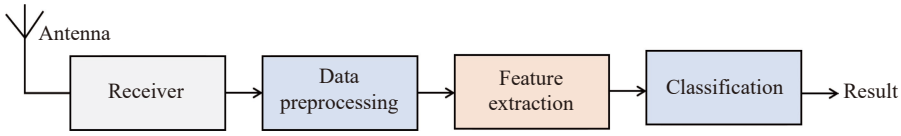

Fig. 1 Typical RFF system

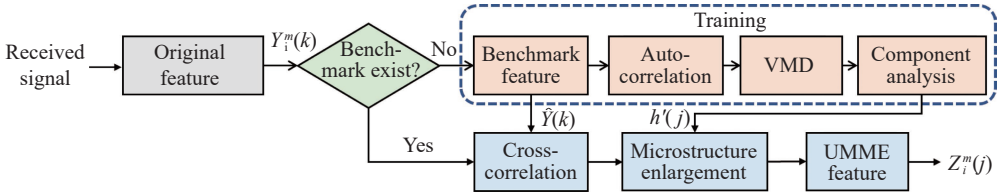

Fig. 2 Flowchart of the proposed UMME method

3.1 Original feature

The instantaneous parameters of signal $s(t)$ include instantaneous amplitude (IA) $A(t)$, instantaneous phase (IP) $\phi(t)$, and instantaneous frequency (IF) $f(t)$, which are defined as

$$\begin{cases} A(t)=\left|s(t)+\mathrm{j}H[s(t)]\right| \\ \phi(t)=\ \mathrm{angle}\ (s(t)+\mathrm{j}H[s(t)]) \\ f(t)=\dfrac{1/2\pi\mathrm{d}\phi(t)}{\mathrm{dt}} \end{cases} \tag{13}$$

where $|\cdot|$ is the l_2-norm; $H[\cdot]$ is the Hilbert Transform, characterized by

$$H[s(t)]=\int_{-\infty}^{+\infty}\frac{s(\tau)}{\pi(t-\tau)}\mathrm{d}\tau=s(t)*\frac{1}{\pi t}. \tag{14}$$

For the analytic discrete-time series $\hat{s}(t)=H[s(t)]$, the arctangent phase $\phi(t)$ can be given as

$$\phi(t)=\arctan\frac{q(t)}{i(t)} \tag{15}$$

where $q(t)$ and $i(t)$ are the real and imaginary components of $\hat{s}(t)$; N_T is the length of $\phi(t)$.

Calculate the phase difference $\Delta\varphi(t)$ between two points, and map $\Delta\varphi(t)$ into $(-\pi,\pi]$ to get

$$\triangle\varphi(t)=\begin{cases}\triangle\phi(t)-2\pi, & \triangle\phi(t)>\pi\\ \triangle\phi(t)+2\pi, & \triangle\phi(t)<-\pi\\ \triangle\phi(t), & \triangle\phi(t)\in[-\pi,\pi]\end{cases}. \tag{16}$$

Calculate $\delta(t)=\triangle\varphi(t)-\triangle\phi(t)$ point by point to obtain the correction amount of the phase difference $\delta(t)$ between adjacent samples. The unwrapping phase $\phi_u(t)$ can be expressed as

$$\phi_u(t)=\phi(t)+\sum_{k=0}^{t-1}\delta(k). \tag{17}$$

In [34], the performance of IF and IP was compared, and the conclusion that IP is better than IF in unique radio device identification is given. IA is susceptible to the noise and multi-path effects. Similar to [35], the instantaneous phase $\phi_u(t)$ is chosen as the original feature [10]. Note that the UIM enlargement method proposed in this paper is not limited to the IP feature.

3.2 Benchmark feature calculation

Let $Y(k)$ $(k=0,1,\cdots,K)$ denote the original RFF feature, while K is the dimension of the feature. As mentioned above, the original feature $Y(i)$ is the combination of IM and UIM. IM is undoubtedly a common characteristic of every emitter while UIM denotes the individual differences among them. To enhance the intuitiveness of this process and to fully incorporate the emitter identity tags, the features can be rewritten as follows:

$$\{Y_i^m(k)\},\quad m=1,\cdots,M;\ i=1,\cdots,N_m;k=0,1,\cdots,K$$

where m represents the mth emitter and N_m is the sample number of the mth emitter.

To accurately reflect the main trend of the features, outliers are deleted based on normalized residual method [28].

Let $\hat{Y}$ be the weighted accumulation of all training sequences [22], which reflect the basic distribution of the original feature $\{Y_i^m(k)\}$.

$$\hat{Y}(k)=\sum_{m=1}^{M}\alpha_m\cdot\mathrm{E}\{Y_i^m(k)\},\quad k=0,1,\cdots,K \tag{18}$$

where α_m represents the weighting coefficients for the mth emitter which satisfies

$$\sum_{m=1}^{M}\alpha_m=1,$$

and K is the dimension of the current feature. The coefficient α_m can be calculated by the distribution of features. For instance, the weight of features with lower PEs than other features can be set to be smaller. In general, the features of different transmitters are equally weighted.

Therefore, $\hat{Y}(k)$ is utilized as a benchmark feature in this algorithm.

3.3 Autocorrelation and cross-correlation

To properly reflect the similarity while enlarging the difference between two signals, which are essentially identical in the outline, we use a correlation algorithm.

The autocorrelation function $\hat{R}(j)$ of the benchmark feature $\hat{Y}(k)$ can be defined as

$$\hat{R}(j)=\Re\{\hat{Y}(k),\hat{Y}(k)\},\quad j=0,1,\cdots,J \tag{19}$$

where J is the length of the result, $J=2K-1$, $\Re\{\cdot,\cdot\}$ represents the correlation operation:

$$R(n)=\Re\{x(m),y(m)\}=\sum_{m=-\infty}^{\infty}x(m)y(n+m).$$

We calculate the cross-correlation result $R_i^m(j)$ between each sequence $Y_i^m(k)$ and the benchmark feature $\hat{Y}(k)$ here as follows:

$$R_i^m(j)=\Re\{Y_i^m(k),\hat{Y}(k)\} \tag{20}$$

where $R_i^m(j)$ is the correlation feature for the ith sequence of the mth emitter and j is the dimension of the current feature.

3.4 VMD and component analysis

Decompose $\hat{R}(j)$ in (20) self-adaptively using VMD:

$$\{\boldsymbol{V},\widehat{\boldsymbol{V}},\boldsymbol{\Omega}\}=\mathrm{VMD}\{\hat{R}(j),L\} \tag{21}$$

where $\mathrm{VMD}\{\cdot,\cdot\}$ represents the VMD operation in Subsection 2.2, L is the number of modes, $\boldsymbol{V}$ is the time mode matrix, $\widehat{\boldsymbol{V}}$ is the spectral mode matrix, and $\boldsymbol{\Omega}$ is the series of the center frequencies.

The VMD results can be more clearly expressed as

$$\begin{cases}\boldsymbol{V}=[v_1(j),v_2(j),\cdots,v_L(j)]\\ \widehat{\boldsymbol{V}}=[\hat{v}_l(j),\hat{v}_2(j),\cdots,\hat{v}_L(j)]\\ \boldsymbol{\Omega}=[\omega_1,\omega_2,\cdots,\omega_L]\end{cases} \tag{22}$$

where $j=1,2,\cdots,J$, $v_l(j)$ represents the lth time mode (namely, IMF); $\hat{v}_l(j)$ is the lth spectral mode, and ω_l is the center frequency of the lth mode.

Therefore, $\hat{R}(j)$ can be written as

$$\hat{R}(j)=\sum_{l=1}^{L}v_l(j) \tag{23}$$

where L is the number of decomposed modes, and $v_l(j)$ is the IMFs with different amplitudes and center frequencies.

IMFs $v_l(j)(l=1,2,\cdots,L)$ can be sorted by energy value and frequency. IMFs with the highest energy and lowest center frequency (potentially the same individual IMF) are selected as the representatives for IM. Similarly,

the correlation features $R_i^m(j)$ are scrupulously decomposed by the above methods. All chosen IMFs with weights assigned by (18) are accumulated and placed with $\hat{v}_l$ into the corresponding results set ℓ.

Let $h(j)$ be the sum of these representative IMFs, which can be defined as

$$h(j)=\sum_{\hat{v}_l\in\ell}\hat{v}_l(j). \tag{24}$$

3.5 Microstructure enlargement

Another VMD is performed, and the IMF with the highest center frequency is regarded as a high-frequency stray item, which is added into the set ℓ, $h(j)$ is updated as $h'(j)$. As mentioned above, $h(j)$ is the essential common component of all $R_i^m(j)$ conforming to the basic characteristics of IM, so $h'(j)$ can be expressed as $(\mathrm{IM}+\varepsilon)$, where ε is the decomposition error.

Further, the final UMME feature $Z_i^m(j)$ of the ith sequence for the mth emitter can be written as

$$Z_i^m(j)=R_i^m(j)-h'(j)=R_i^m(j)-\sum_{\hat{v}_l\in\ell}\hat{v}_l(j) \tag{25}$$

where j is the feature dimension.

As described in Subsection 2.1, the final feature F^{UIM} can be abstracted as

$$F^{\mathrm{UIM}}=S^m-(\mathrm{IM}+\varepsilon)=\mathrm{UIM}^m+\varepsilon \tag{26}$$

where $\mathrm{IM}>>\mathrm{UIM}^m$ and $\mathrm{UIM}^m>\varepsilon$. The algorithm improves the proportion of UIM energy in the final feature and amplifies the UIM in terms of effect.

3.6 Computation analysis

The whole system can be divided into two parts which include two different types of VMD and the correlation computation. In the training phase (given as the upper branch in Fig. 2, the VMD decomposes the autocorrelation of the benchmark to obtain the main trend; this requires only one round of training. The cross-correlation feature between the original feature and the benchmark feature is decomposed by anther VMD to obtain the stray item. This procedure is conducted separately for each sequence.

Therefore, for each original feature, the main computation burden of the proposed method arises from one VMD and cross-correlation operation. In the VMD stage, $O(J\times L\times T)$ operations are required, where J is the feature dimension, L is the number of the modes, and T is the iterations [22]. For cross-correlation, it is linear with the feature dimension J, namely, $O(J)$. Overall, the main computational burden is $O(J\times L\times T)$.

4. Experimental results

Experiments based on real-world data are conducted to evaluate the proposed method. Note that this work focuses more on the enlargement of the subtle UIM contained in RFF features, instead of extracting newly-defined features. More attention is paid to the improvement of original feature performance for RFF in this section.

4.1 Dataset

Real-world signals emitted by secondary surveillance radars (SSRs) of 20 civil aircrafts working in Mode S are used to test the effectiveness of the proposed method. All signals have the same intra-pulse intentional modulation [36]. The channel environment and receiving equipment remain unchanged during signal reception. The sampling frequency is set to 250 MHz and the sampling intermediate frequency to 60 MHz. At least 300 samples of high quality are gathered for each SSR emitter. For 20 transmitters, there are a total of 6 210 samples. The configuration parameters are listed in Table 1.

Table 1 Configuration parameters

Parameter	Value
Radio frequency/MHz	1 090
Sample frequency/MHz	250
Intermediate frequency/MHz	60
Samplesper/transmitter	⩾300
Transmitter ID	R01 to R20

4.2 Visualization and computational time

The original feature distributions of emitters R1 and R3 as examples are shown in Fig. 3.

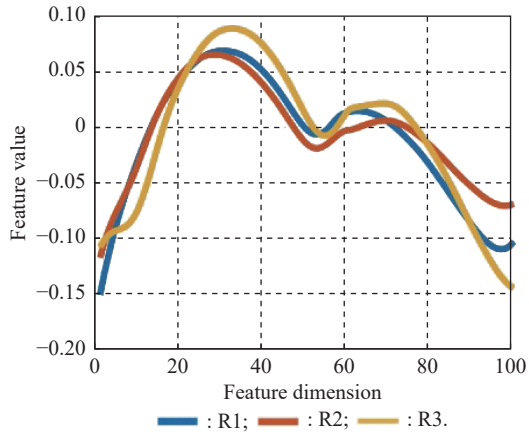

Fig. 3 Original feature curves of emitters R1−R3

There is a high degree of similarity between the shapes of the curves with a few local and weak differences

reflecting device-specific information. R2 and R3 can be discriminated by the feature value between 20−40 on the abscissa; the feature value of R1 at 80−100 is different from R2. Although it can be classified with the naked eye, the differences between classes are not yet sufficiently obvious. As the number of transmitters increases, the difficulty of identification will increase greatly.

The curves of the benchmark feature and its four IMFs after VMD are shown in Fig. 4, where the horizontal axis represents the feature dimension and the vertical axis is features values. The top subgraph shows the autocorrelation curve of the benchmark feature; others are the decomposed components, that is IMF1−IMF4.

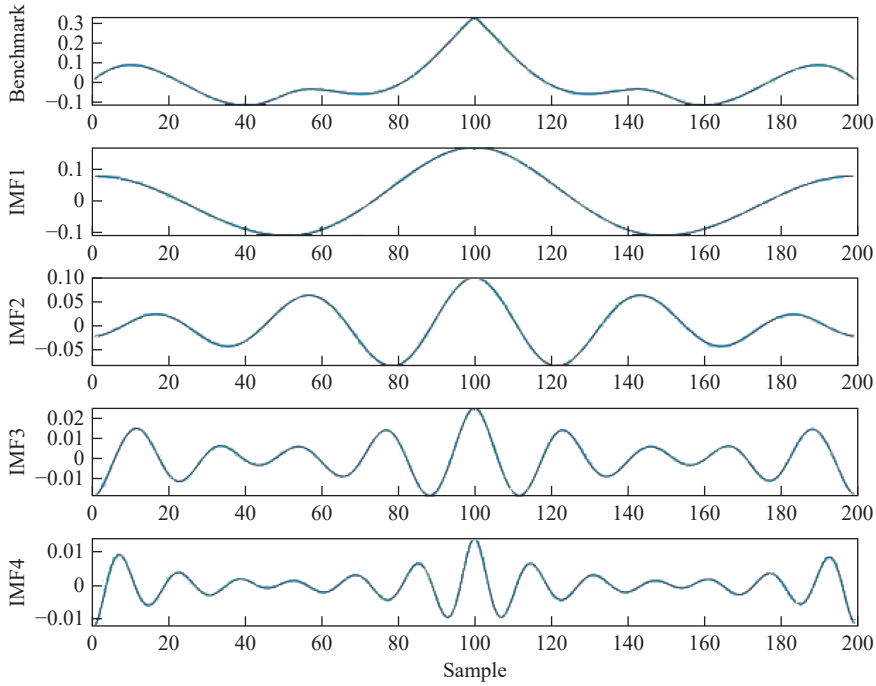

Fig. 4 Schematic diagram of VMD benchmark feature autocorrelation $\hat{R}(j)$ decomposition

The UMME feature curves of emitters R1 to R3 after enlarging the UIM microstructures via the proposed method are shown in Fig. 5. The individual differences are significantly magnified compared to those in the original curves.

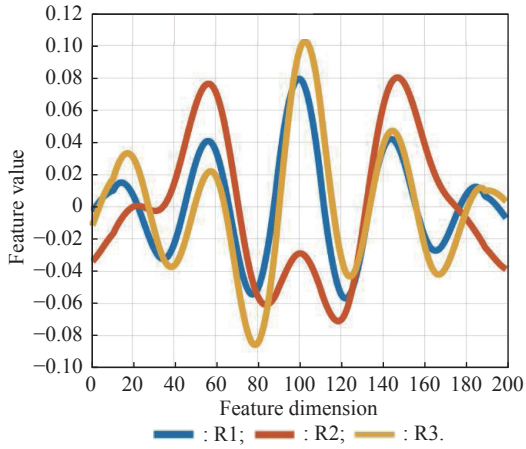

Fig. 5 UMME feature curves of emitters R1 to R3, UIM microstructures enlarged by proposed method

Additionally, we record the average computational ti me of different processes per sample, as listed in Table 2. These experiments are performed on a computer with an i5 processor, 8 GB of RAM. Its computational burden mainly comes from VMD.

Table 2 Computational time s

Process	Time
Auto-correlation	0.012
Cross-correlation	0.013
VMD	0.210
Original feature	0.073

Consistent with the above analysis, the computational burden mainly comes from VMD, but this process only needs to be done once in the training phase. Only the original feature calculation and cross-correlation calculation are required for one sample in the identification phase.

4.3 Numerical results

4.3.1 Feature changes between emitters

Three evaluation indexes, PE, ED, and MI, are used to quantitatively describe the similarities and differences of features to determine the effectiveness of the proposed algorithm. The results for the five emitters R1−R5 are given in Table 3−Table 8, where the content represents the corresponding index value of two emitters. $f = F(R_i \cdot R_j)$ where $F(\cdot)$ is abbreviation of the indexes in (10)−(12) and i, j represent the ith and jth emitters respectively ($i \neq j$). For instance, the value 0.972 in Table 3 means that the PE of the original features between emitters R1 and R2 is 0.972.

Table 3 PE of pairwise emitters for original features of R1−R5

f	R2	R3	R4	R5
R1	0.972	−0.881	0.959	0.940
R2	−	−0.879	0.942	0.910
R3	−	−	−0.727	−0.864
R4	−	−	−	0.869

Table 4 PE of pairwise emitters for UMME features of R1−R5

f	R2	R3	R4	R5
R1	0.545	−0.316	0.921	0.763
R2	−	0.601	0.42	0.919
R3	−	−	−0.344	0.316
R4	−	−	−	0.587

Table 5 ED of pairwise emitters for original features of R1−R5

f	R2	R3	R4	R5
R1	0.177	1.008	0.197	0.234
R2	−	0.879	0.284	0.184
R3	−	−	1.047	0.844
R4	−	−	−	0.366

Table 6 ED of pairwise emitters for UMME features of R1−R5

f	R2	R3	R4	R5
R1	0.694	2.446	0.340	0.470
R2	−	1.778	0.861	0.295
R3	−	−	2.545	2.013
R4	−	−	−	0.701

Table 7 MI of pairwise emitters for original features of R1−R5

f	R2	R3	R4	R5
R1	0.852	0.815	0.867	0.805
R2	−	0.804	0.860	0.814
R3	−	−	0.822	0.791
R4	−	−	−	0.825

Table 8 MI of pairwise emitters for UMME features of R1−R5

f	R2	R3	R4	R5
R1	0.724	0.706	0.708	0.733
R2	−	0.744	0.731	0.778
R3	−	−	0.720	0.739
R4	−	−	−	0.740

Table 3 and Table 4 show the changes in PE values between the original features and final features. The PE between the original features is relatively high and concentrated at about 0.9, which is consistent with the previous expression that the fingerprint features are highly similar. After amplifying the individual differences by the proposed method, the PE value is greatly reduced. Table 5 and Table 6 illustrate the results of the average ED between different features of various emitters, where there is a dramatic increase in the distance between different classes. Table 7 and Table 8 show the MI values, which relate to the changes of dependence between the features. For UMME feature, the MI between pairwise emitters obviously declines. These three indicators altogether indicate that a significant improvement in the feature distribution after the proposed algorithm is imposed and the device-specific difference is distinctly enlarged.

4.3.2 Overall change of features

The normalized difference description index values of fingerprint features under different target numbers of radiation sources I (I=3,5,10,15,20) is shown in Table 9, where X represents the original IP feature, Y 0 is the enlarged feature without correlation calculation, and Y is the enlarged UMME feature calculated by the proposed method.

The values in the table are the average values of different combinations of normalized parameters between pairs of all targets, which can be expressed as

$$\tilde{f} = \frac{1}{M'} f_{ij} = \frac{1}{M'} \sum_{i=1}^{I} \sum_{j=1}^{I} F(R_i \cdot R_j), i \neq j \qquad (27)$$

where M' indicates the total number of pairwise combinations C_I^2. The first row of the table (I=3) shows the changes in the evaluation indexes of the features of the three transmitters in Fig. 3 and Fig. 5.

As can be seen in Table 9, the degree of correlation PE between features significantly decreases to about 0.6, while the distance expands to more than twice the original at an average of 2.4 times. The amount of MI also decreases significantly. In the case of different number of targets, the changes in the three indexes all indicate that the subtle structure between the characteristic curves is enlarged after operating the proposed method. In effect, our algorithm is valid.

Without performing correlation operations, that is,

while only performing feature amplification by removing the intentional modulation and spurious components after VMD decomposition, as shown as *Y*0 in Table 9, the distance of the features does not change significantly and the mutual information does not decrease. Although the correlation degree of the characteristic curve (PE) decreases, the effect is similar to the proposed correlation magnification method; there is no obvious superiority.

Table 9 Feature similarity, distance, and dependency metrics for various numbers of emitters (*I*=3,5,10,15,20)

$\tilde{f}$	PE			ED			MI		
	X	*Y*0	*Y*	*X*	*Y*0	*Y*	*X*	*Y*0	*Y*
I=3	0.958	0.678	0.609	0.220	0.266	0.632	0.86	0.861	0.740
I=5	0.894	0.539	0.573	0.522	0.524	1.214	0.826	0.842	0.732
I=10	0.745	0.530	0.567	0.537	0.550	1.235	0.820	0.833	0.735
I=15	0.637	0.543	0.568	0.598	0.600	1.396	0.817	0.841	0.732
I=20	0.641	0.546	0.577	0.583	0.590	1.349	0.817	0.836	0.733

4.3.3 Improvement on identification accuracy

The identification performance of the original features and the proposed UMME features for various emitters (*I*=5,10,15,20) after 200 Monte Carlo simulation is shown in Fig. 6. The Gaussian mixture model (GMM) classifier is chosen for classification [37]. The accuracy is calculated as the average value of all emitters of all trials. Due to the proposed UIM enlargement analysis method, the identification accuracies markedly improve in all cases of various numbers of emitters, which verifies its effectiveness. When *I*=20, the recognition rate increases by 4%.

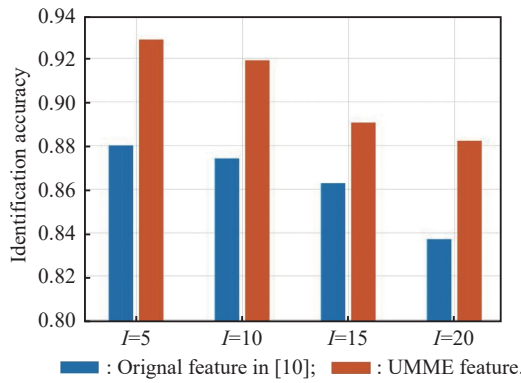

Fig. 6 Identification performance of various numbers of emitters for original feature in [10] and UMME feature

The 3-dimensional (3D) feature distribution in the case of *I* = 10 (emitters R1 to R10) after t-distribution stochastic neighbour embedding (t-SNE) method is illustrated in Fig. 7. It can be seen that all emitters can be clearly differentiated.

In addition, we test the influence of the numbers of the Gaussian models and the setting of benchmark features on the identification accuracy under 10 dB. The impact of GMM models is given in Fig. 8. As can been seen, as the model number grows more than 10, the accuracy degrades rapidly. When there are 4 or 6 GMM models, the influence of the setting of benchmark feature is illustrated in Table 10, where "R1" and "R4" represent that the average feature of emitter R1 or R4 is chosen as benchmeark feature, and $\hat{Y}(k)$ is for the method proposed in Subsection 3.2. It can be seen that our proposed benchmark calculation method is better for both 5 and 10 emitters.

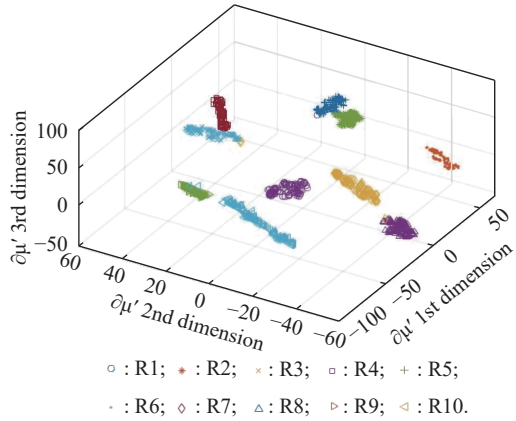

Fig. 7 UMME function distribution of R1−R10 after dimensionality reduction by t-SNE algorithm

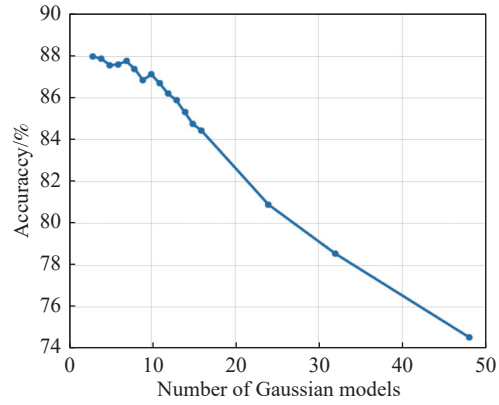

Fig. 8 Identification performance of various numbers of Gaussian models of the GMM when *I*=10 under 10 dB

Table 10 Identification accuracy of different benchmark features under 10 dB

%

Benchmark feature	4 GMM		6 GMM	
	I=5	I=10	I=5	I=10
R1	90.640	67.378	92.836	74.132
R4	91.728	69.652	93.704	75.998
$\hat{Y}(k)$	93.248	70.762	94.992	76.678

4.3.4 Comparison with other works

The identification performance in additive white Gaussian noise (AWGN) channel compared with other works is examined, as illustrated in Fig. 9. This experiment is based on 10 transmitters (R1−R10) after 200 Monte Carlo simulation. AWGN is added to the signals, and the signal to noise ratio (SNR) ranges from 10 dB to 20 dB. Different numbers (10 or 20) of outliers are deleted when calculating benchmark features. OIP-x in Fig. 9 represents a method without UIM enlargement, where UMME-x is the proposed one (x represents 10 or 20 outliers). In this experiment, it can be seen that this method is better than other methods under various SNRs. Compared with the OIP-x, the performance improvement of the UMME-x proves the superiority of the UIM enlargement strategy.

Additionally, we also compare the proposed method with the DL-based method, which is based on the convolutional neural network (CNN). The layers of the identification baseline CNN are similar to [5,38], referred to as DL in this work.

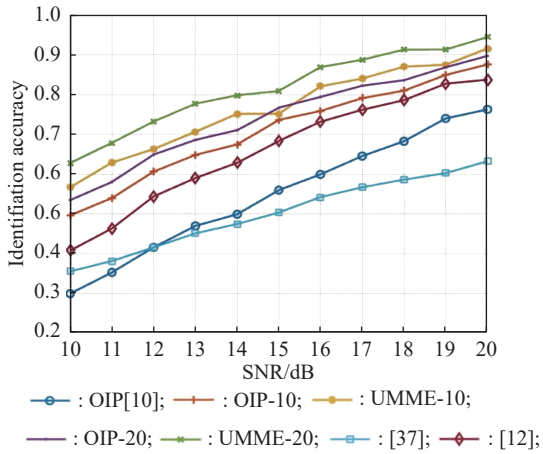

Fig. 9 Identification performance of different algorithms with different SNRs

The input of DL is the received signal waveforms and the output is the predicted class label. In the experiment, the size of the training dataset is set according to the requirements ranging from 50 to 200 per class. There are 50 samples per class selected as the test dataset and 50 samples as the validation set. The setting on the dataset of the UMME algorithm is consistent with that of DL. The rest of the parameter settings are the same as above. The training accuracy and loss of DL are shown in Fig.10.

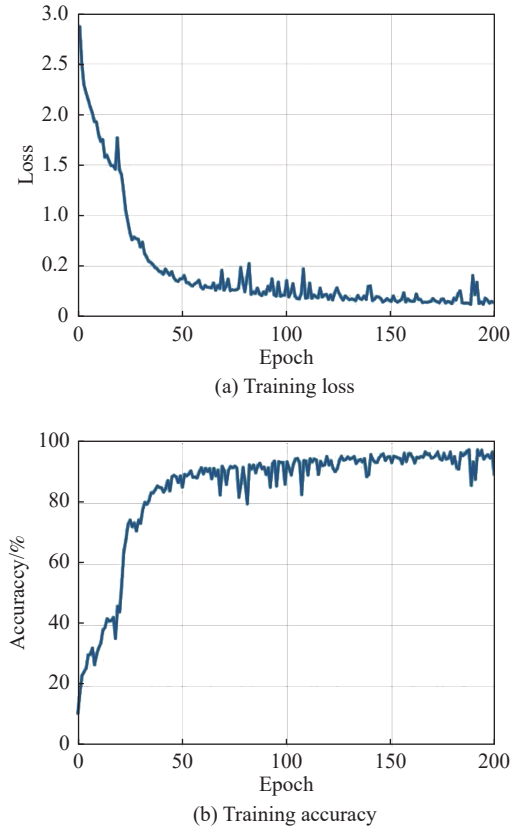

Fig. 10 Training loss and accuracy of DL

The performance of the UMME and Net on the validation dataset under different SNRs and training data sizes are shown in Fig.11. Numbers in the legend mean the training data size per class, that is the number of samples in the training set of each class.

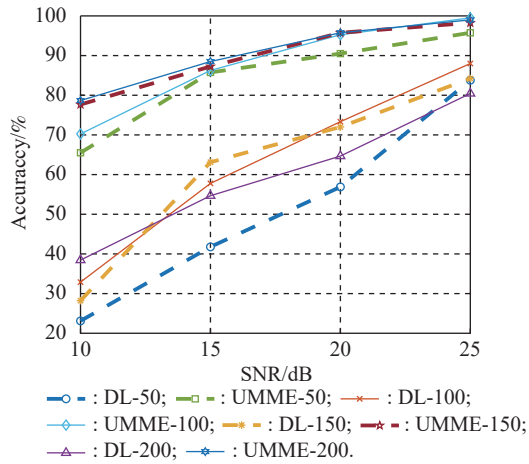

Fig. 11 Identification performance of UMME and DL with different SNRs of R1−R10

It can be seen that the proposed UMME outperforms DL. When the SNR degrades, the performance decline of UMME is relatively flat. However, DL drops faster which indicates that the performance of DL has a higher requirement on the signal quality. And there is no significant performance difference of UMME with respect to the training data size, which shows that UMME is not sensitive to the changes in the number of the training samples. Since the training scale is small (no more than 200), DL, as a data-driven method, does not work robustly, and its performance curves are relatively scattered. However, in the actual application of RFF, the effective data available for training is generally limited, and due to the complicated receiving environment, the signal quality is hard to guarantee. Therefore, UMME is more accurate and practical than DL.

5. Conclusions

In RFF, individual-specific UIM information is more important, but it is relatively small and submerged in intentional modulation. To reduce the influence of IM and expand the miniscule differences between emitters for RFF, a UMME method is developed in this study to enlarge the microstructures of the extracted UIM based on feature-level VMD. PE, ED, and MI indexes are utilized to respectively quantify the similarity, distance, and dependency of the RFF features from different emitters. Experiments based on real-world data qualitatively and quantitatively demonstrate that the proposed method magnifies subtle differences, reduces the similarity, and improves the independency among UIM features. Finally, the GMM-based identification experiments verify the performance improvement of the proposed algorithm on RFF. In addition to being inherently suitable for RFF feature distribution, the working concept of UMME could also be applied to other types of RFF features, signals, and scenes in the future.

References

[1] XIE F Y, WEN H, WU J S, et al. Data augmentation for radio frequency fingerprinting via pseudo-random integration. IEEE Trans. on Emerging Topics in Computational Intelligence, 2020, 4(3): 276–286.

[2] BECKER J K, GVOZDENOVIC S, XIN L X, et al. Testing and fingerprinting the physical layer of wireless cards with software-defined radios. Computer Communications, 2020, 160(4): 186–196.

[3] DOBRE O A. Signal identification for emerging intelligent radios: classical problems and new challenges. IEEE Instrumentation & Measurement Magazine, 2015, 18(2): 11–18.

[4] WANG W H, SUN Z, PIAO S, et al. Wireless physical-layer identification: modeling and validation. IEEE Trans. on Information Forensics and Security, 2016, 11(9): 2091–2106.

[5] MERCHANT K, REVAY S, STANTCHEV G, et al. Deep learning for RF device fingerprinting in cognitive communication networks. IEEE Journal of Selected Topics in Signal Processing, 2018, 12(1): 160–167.

[6] DAVASLIOGLU K, SOLTANI S, ERPEK T, et al. Deep-WiFi: cognitive WiFi with deep learning. IEEE Trans. on Mobile Computing, 2021, 20(2): 429–444.

[7] LIN Y, JIA J C, WANG S, et al. Wireless device identification based on radio frequency fingerprint features. Proc. of the IEEE International Conference on Communications, 2020. DOI:10.1109/ICC40277.2020.9149226.

[8] ZHOU Y P, WANG X, CHEN Y, et al. Specific emitter identification via bispectrum-radon transform and hybrid deep model. Mathematical Problems in Engineering, 2020, 2020: 7646527.

[9] TALBOT K I, DULEY P R, HYATT M H. Specific emitter identification and verification. Technology Review Journal, 2003. https://www.researchgate.net/publication/228790296_Specific_emitter_identification_and_verification.

[10] RU X H, LIU Z, HUANG Z T, et al. Recognition performance analysis of instantaneous phase and its transformed features for radar emitter identification. IET Radar, Sonar & Navigation, 2016, 10(5): 945−952.

[11] SUN L T, WANG X, YANG A F, et al. Radio frequency fingerprint extraction based on multi-dimension approximate entropy. IEEE Signal Processing Letters, 2020, 27: 471−475.

[12] RU X H, LIU Z, HUANG Z T, et al. Evaluation of unintentional modulation for pulse compression signals based on spectrum asymmetry. IET Radar, Sonar & Navigation, 2017, 11(4): 656−663.

[13] WILSON A J, REISING D R, LOVELESS T D. Integration of matched filtering within the RF-DNA fingerprinting process. Proc. of the Global Communications Conference, 2019. DOI:10.1109/GLOBECOM38437.2019.9014225 .

[14] SATIJA U, TRIVEDI N, BISWAL G, et al. Specific emitter identification based on variational mode decomposition and spectral features in single hop and relaying scenarios. IEEE Trans. on Information Forensics and Security, 2019, 14(3): 581−591.

[15] ZHANG J W, WANG F G, DODRE O A, et al. Specific emitter identification via Hilbert–Huang transform in single-hop and relaying scenarios. IEEE Trans. on Information Forensics and Security, 2016, 11(6): 1192–1205.

[16] SEDDIGHI Z, AHMADZADEH M R, TABA5N M R. Radar signals classification using energy-time-frequency distribution features. IET Radar, Sonar & Navigation, 2020, 14(5): 707–715.

[17] BALAKRISHNAN S, GUPTA S, BHUYAN A, et al. Physical layer identification based on spatial-temporal beam features for millimeter-wave wireless networks. IEEE Trans. on Information Forensics and Security, 2020, 15: 1831–1845.

[18] PENG L N, ZHANG J Q, LIU M, et al. Deep learning based RF fingerprint identification using differential constellation trace figure. IEEE Trans. on Vehicular Technology, 2020, 69(1): 1091–1095.

[19] LI L, JI H B. Radar emitter recognition based on cyclostationary signatures and sequential iterative least-square estimation. Expert Systems with Applications, 2011, 38(3): 2140–2147.

[20] ROY D, MUKHERJEE T, CHATTERJEE M, et al. RFAL: adversarial learning for RF transmitter identification and classification. IEEE Trans. on Cognitive Communications and Networking, 2020, 6(2): 783–801.

[21] SANKHE K, BELGIOVINE M, ZHOU F, et al. No radio left behind: radio fingerprinting through deep learning osf physical-layer hardware impairments. IEEE Trans. on Cognitive

Communications and Networking, 2020, 6(1): 165–178.
[22] GOK G, ALP Y K, ARIKAN O. A new method for specific emitter identification with results on real radar measurements. IEEE Trans. on Information Forensics and Security, 2020, 15: 3335–3346.
[23] YE H, LIU Z, JIANG W L. Comparison of unintentional frequency and phase modulation features for specific emitter identification. Electronics Letters, 2012, 48(14): 875–877.
[24] CHEN P B, GUO Y L, LI G, et al. Adversarial shared-private networks for specific emitter identification. Electronics Letters, 2019, 56(1): 296–299.
[25] WU L W, NIU J P, WANG Z, et al. Primary signal suppression based on synchrosqueezed wavelet transform. Journal of Electronics & Information Technology, 2019, 42(8): 2045–2052.
[26] CHEN P B, GUO Y L, LI G. Discriminative adversarial networks for specific emitter identification. Electronics Letters, 2020, 56(9): 438–441.
[27] FENG Z P, ZHANG D, ZUO M J, et al. Adaptive mode decomposition methods and their applications in signal analysis for machinery fault diagnosis: a review with examples. IEEE Access, 2017, 5: 24301–24331.
[28] WU L W, ZHAO Y Q, FENG M F, et al. Specific emitter identification using IMF-DNA with a joint feature selection algorithm. Electronics, 2019, 8(9): 934.
[29] LIANG J H, HUANG Z T, YUAN Y J, et al. A method based on empirical mode decomposition for identifying transmitter individuals. Journal of CAEIT, 2013, 8(4): 393–417.
[30] KAY S M. Fundamentals of statistical signal processing. Englewood: PTR Prentice Hall, 1993.
[31] DRAGOMIRETSKIY K, ZOSSO D. Variational mode decomposition. IEEE Trans. on Signal Processing, 2014, 62(3): 531–544.
[32] ROY D, MAINAK T, CHATTERJEE M, et al. RF transmitter fingerprinting exploiting spatio-temporal properties in raw signal data. Proc. of the IEEE 18th International Conference on Machine Learning and Applications, 2019.
[33] SUN J X. Modern pattern recognition. Beijing: Higher Education Press, 2008.
[34] CHEN P B, XU K, LI K, et al. Local frechet distance in specific emitter identification. Proc. of the IEEE 9th International Conference on Communication Software and Networks, 2017. DOI:10.1109/ICCSN.2017.823023
[35] CHEN P B, XU K, LI K, et al. Local frechet distance in specific emitter identification. Proc. of the IEEE 9th International Conference on Communication Software and Networks, 2017. DOI:10.1109/ICCSN.2017.8230230.
[36] LEONARDI M, FAUSTO D D. Secondary surveillance radar transponders classification by RF fingerprinting. Proc. of the 19th International Radar Symposium, 2018: 1−10. DOI: 10.23919/IRS.2018.8448244.
[37] CHEN S T, JIANG Q C, YAN X F. Multimodal process monitoring based on transition-constrained Gaussian mixture model. Chinese Journal of Chemical Engineering, 2020, 28(12): 3070–3078.
[38] YU J B, HU A Q, LI G Y, et al. A multi-sampling convolutional neural network-based RF fingerprinting approach for low-power devices. Proc. of the IEEE INFOCOM Conference on Computer Communications Workshops, 2019: 1–6.

Biographies

SUN Liting was born in 1994. She received her B.E. degree from the School of Information Science and Engineering, Shandong University, Ji'nan, China, in 2017. She is currently pursuing her Ph.D. degree with State Key Laboratory of Complex Electromagnetic Environment Effects on Electronics and Information System, National University of Defense Technology, Changsha, China. Her current research interests include cognitive radio, signal processing, and physical-layer security.
E-mail: slt2009@yeah.net

WANG Xiang was born in 1985. He received his B.S. and Ph.D. degrees in electronic science and engineering from the National University of Defense Technology, Changsha, Hunan, China, in 2007 and 2013, respectively, where he is currently an associate professor with the College of Electronic Science and Engineering. His research interests include blind asignal processing in radar and communication applications and pattern recognition.
E-mail: christopherwx@163.com

HUANG Zhitao was born in 1976. He received his B.S. and Ph.D. degrees in information and communication engineering from the National University of Defense Technology, Changsha, Hunan, China, in 1998 and 2003, respectively, where he is currently a professor with the College of Electronic Science and Engineering. His research interests include radar and communication signal processing and array signal processing.
E-mail: huangzhitao@nudt.edu.cn